Piezoelectric Energy Harvesting from Composite Beams in Geometric Nonlinear Regime: Numerical and Experimental Approach

Grigoris C. Kardarakos[a], Nikolaos A. Chrysochoidis[a], Dimitris Varelis[c], Dimitris A. Saravanos[a], Theofanis S. Plagianakos[1b], Panagiotis Vartholomeos[b], Nikolaos Leventakis[b], G. Bolanakis[b], Nikolaos Margelis[b], Evangelos G. Papadopoulos[b]

[a]Structural Analysis and Adaptive Materials Group, Dept. of Mechanical and Aeronautical Engineering, University of Patras, 26500 Patras, Greece; [b]Control Systems Lab, School of Mechanical Engineering, National Technical University of Athens, 15780 Athens, Greece, [c]Department of Aeronautical Sciences, Hellenic Air Force Academy, 13672 Athens, Greece

ABSTRACT

Energy harvesting from oscillating structures receives a lot of research attention as these applications appear promising for the continuous energy supply of low power devices. Recent studies indicate increased power production of piezoelectric energy harvester configurations undergoing severe nonlinear vibrations, but the obvious drawback is the increased complexity of the coupled electromechanical dynamic response of the harvester. The current study focuses on the development of a robust and accurate numerical tool capable of modelling and design of such systems. This model is used to simulate the electromechanical response of composite strip structures equipped with piezoelectric devices subjected to nonlinear oscillations under compressive loading and near buckling instability conditions. The study is combined with experimental verification studies on a fabricated harvester prototype aiming to validate the numerical tool and to corroborate the electrical voltage generation on the piezoelectric devices. Additionally, a preliminary experimental study is performed to quantify the available electrical energy that is produced from the oscillating structure. Three different harvesting circuits are studied and their energy conversion performance is investigated. Measured results validate the developed numerical tool. Moreover, the increased electrical voltage and charge generation during the geometrically nonlinear oscillations as the prebuckling load increases, increasing also the available electrical power on the circuits, is illustrated numerically and experimentally.

Keywords: composites, piezoelectric energy harvesting, geometric nonlinearity

1. INTRODUCTION

In the last two decades piezoelectric energy harvesting (PEH) has been an active research and development field for low-power devices in the context of Internet of Things (IoT) and relevant applications. Over the past decade it has been shown that the piezoelectric energy harvesting (PEH) capacity is enhanced when the host structure undergoes large displacements and rotations during vibration, as in the case of bistable structural systems[1]-[2]. Besides improved power harvesting capabilities, nonlinear systems enable efficient performance over an extended excitation frequency bandwidth compared to linear systems, as initially observed in cantilever PEH beams undergoing magnetic levitation[3]-[5]. While several deformation mechanisms leading to nonlinear response have been derived for emerging applications[6]-[7], buckled beam configurations seem to be most prominent for highest power harvesting in the case of low-frequency excitation[8]. The current work focuses on PEH from a vibrating wind turbine blade[9], thus falling into the latter configuration category, which is shortly surveyed in the following paragraph.

The proof of concept of an axially compressed piezoelectric energy harvester has been derived by Leland and Wright[10]. Sneller et al.[11] studied the effect of central mass on open-circuit voltage of a clamped-clamped steel beam subjected to harmonic base excitation. A similar configuration has been numerically and experimentally studied by Masana and

[1] fanplag@gmail.com; phone 30 2107722348; https://www.enausi-project.gr/en/

Active and Passive Smart Structures and Integrated Systems XV, edited by Jae-Hung Han, Gang Wang, Shima Shahab, Proc. of SPIE Vol. 11588, 115881D · © 2021 SPIE · CCC code: 0277-786X/21/$21 · doi: 10.1117/12.2582767

Daqaq[12], who developed a continuum model based on nonlinear Euler-Bernoulli beam theory. Cottone et al.[13] applied first-order shear kinematics and compared the response in nonlinear bistable and linear stable dynamic regime under wideband random base excitation. Lumped-parameter models for axially compressed beam configurations have been derived by Ramlan et al.[14] and Liu et al. for single-mode[15] or multi-mode[16] response prediction. Recently, Speciale et al.[17] designed, manufactured and tested a prototype employing a snap-through buckling mechanism. In most of these and relevant works open- or resistive-circuits have been considered. This trend may be justified by the fact that a solid background has been built since the early 2000s on improving the design of electric circuits in order to maximize harvested power by optimizing electromechanical interactions and coupling between the vibrating structure and harvesting circuit[18]-[25]. The majority of reported models are either simplified lumped parameter models or computationally expensive detailed 3D finite element models. It seems that there exist a gap in the available modelling tools that will enable the efficient, yet accurate and detailed enough design, enabling the understanding and optimization of the complex nonlinear dynamic response, and elecromechanical coupling between the vibration structure and the energy harvesting system.

The current paper aims at presenting work in progress on numerical modeling and experimental verification of axially compressed composite beams under dynamic base excitation. Three are the main objectives of the current study; the first is to develop a robust numerical tool based on a reduced-order piezoelectric plate finite element, capable to describe the nonlinear vibrations of piezoelectric composite beams; the second is to demonstrate a prototype configuration for the electrical energy production via nonlinear vibrations assisted by the computational tool in order to tailor the mechanism parameters and third to investigate the energy production from the oscillating structure using appropriate rectification circuits. The developed numerical tool is an integrated (ply-laminate-structure) formulation, based on first-order shear kinematics, encompassing initial stresses and large rotations. The formulation is implemented by means of a finite element approximation at structural level to yield prediction of the coupled electromechanical response in open-circuit configuration. An experimental configuration, designed in the context of the present work, serves for experimental verification of the finite element predictions. In addition, three harvesting circuits have been tested on the experimental set-up to provide an estimate of each individual circuit performance and amount of power that could be harvested.

2. THEORETICAL FRAMEWORK AND NUMERICAL MODELING

In this section, the piezoelectric laminate mechanics and the numerical methods utilized to numerical modeling are introduced. At first, the material of each ply of the piezoelectric laminate structure is assumed to be under the linear regime, whereas the linear piezoelectricity is also adopted. Thus, the constitutive equations which characterize the stress state at ply level are given below.

$$\begin{aligned} \sigma_i &= C_{ij}^{E,T} S_j - e_{ik}^T E_k \qquad && i,j = 1,...6 \\ D_l &= e_{lj}^T S_j + \varepsilon_{lk}^{S,T} E_k \qquad && k,l = 1,..3 \end{aligned} \tag{1}$$

where σ_i, S_i are the mechanical Piola-Kirchhoff stresses and Green's engineering strains in extended vectorial notation respectively, C_{ij} is the elastic stiffness tensor, e_{ik} is the piezoelectric tensor, E_k is the electric field vector, D_l is the electric displacement vector and ε_{lk} is the electric permittivity tensor. Superscripts E, S, T represent constant voltage, strain, and temperature conditions, respectively.

2.1 Kinematic Assumptions

To describe the kinematic assumptions of the state variables, the nonlinear multi-field piezoelectric laminate theory is adopted, which combines first shear deformation assumptions for the displacement field with a linear layerwise electric potential field[28]-[30]. The theory further considers large laminate rotations, according to the Von-Karman nonlinearity assumptions. The equivalent Green-Lagrange strains take the following form:

$$
\begin{aligned}
S_1 &= u^o_{,x} + z\beta_{x,x} + \frac{1}{2} w^{o^2}_{,x} \\
S_2 &= v^o_{,y} + z\beta_{y,y} + \frac{1}{2} w^{o^2}_{,y} \\
S_6 &= u^o_{,y} + v^o_{,x} + z\left(\beta_{x,y} + \beta_{y,x}\right) + w^o_{,x} w^o_{,y} \\
S_4 &= w^o_{,y} + \beta_y \\
S_5 &= w^o_{,x} + \beta_x
\end{aligned}
\tag{2}
$$

where u^o, v^o are the midplane in-plane displacements along the x and y directions, respectively, while w^o is the transverse displacement; β_x and β_y are the bending rotation angles about the y and x axes, respectively. The three last RHS terms of the S_i strains (i=1,2,6) express the nonlinear strain components S_{Li} respectively, with all referred on the mid-surface A_o. The subscript "," denotes spatial derivative in respect to the axis following the subscript.

The approximation of electric fields within a piezoelectric layer which is located between the thickness points z_{m+1} and z_m is provided by the following expressions:

$$
\begin{aligned}
E_1(x,y,z) &= -\left(\Phi^{m+1}_{,x}(x,y)\Psi^{m+1}(z) + \Phi^m_{,x}(x,y)\Psi^m(z)\right) \\
E_2(x,y,z) &= -\left(\Phi^{m+1}_{,y}(x,y)\Psi^{m+1}(z) + \Phi^m_{,y}(x,y)\Psi^m(z)\right) \\
E_3(x,y,z) &= -\left(\Phi^{m+1}(x,y) - \Phi^m(x,y)\right)\Big/ \mathrm{h_m}
\end{aligned}
\tag{3}
$$

where $h_m = z_{m+1} - z_m$ is the thickness of the layer; Φ^{m+1} and Φ^m denote the electric potentials at the corresponding thickness points, and Ψ^m are interpolation functions through the thickness of the piezoelectric laminate.

2.2 Generalized Dynamic Equations of Motion in Variational Form

Based on the Virtual Work principle and neglecting the physical damping of the piezoelectric structure, the equations of motion of the piezoelectric laminate plate, mandate that the work of generalized imbalances between external and internal multifield forces Ψ_u and electric charges Ψ_e, should vanish at equilibrium, at any time t over the volume V of the piezoelectric laminated plate[29]:

$$
\begin{aligned}
\delta\, {}^t u^T\, {}^t\boldsymbol{\Psi}_u &= \int_V \delta\, {}^t S^T\, {}^t\sigma dV + \int_V \delta\, {}^t u^T \rho\, {}^t\ddot{u} dV - \int_V \delta\, {}^t u^T\, {}^t b dV - \int_{\Gamma_\tau} \delta\, {}^t u^T\, {}^t\overline{\tau} d\Gamma = 0 \quad \text{at equilibrium} \\
\delta\, {}^t\varphi^T\, {}^t\boldsymbol{\Psi}_e &= \int_V \delta\, {}^t E^T\, {}^t D dV - \int_{\Gamma_q} \delta\, {}^t\varphi^T\, {}^t\overline{q} d\Gamma = 0 \quad \text{at equilibrium}
\end{aligned}
\tag{4}
$$

where ${}^t b, \rho\, {}^t\ddot{u}$ denote body and inertia body forces respectively, ${}^t\overline{\tau}, {}^t\overline{q}$ are the surface tractions and electrical charge applied on the bounding surface Γ_τ and terminal bounding surface Γ_q, respectively. The overdot represents time derivative.

2.3 Coupled nonlinear plate finite element

An eight-node coupled plate finite element, incorporating the previous coupled mechanics is implemented, which approximates the electromechanical state variables on the reference mid-plane A_o with local interpolation functions[29].

Discrete Dynamic Equations of Motion

Substituting the FE approximation into Eqs. (4), assuming no actuators on the structure and introducing a damping term based on the *Rayleigh Damping* model so as to simulate the physical damping of the piezoelectric structure, the following coupled system of nonlinear discrete equations of motion is derived for time step t, indicated as upper left symbol:

$$
\begin{aligned}
{}^{t}\Psi_u(u,\varphi) &= [M]\,{}^{t}\ddot{u} + [C]\,{}^{t}\dot{u} + \left[{}^{t}K_{uu}(u)\right]{}^{t}u + \left[{}^{t}K_{ue}(u)\right]{}^{t}\varphi - {}^{t}\boldsymbol{R}_b - {}^{t}\boldsymbol{R} = 0 \\
{}^{t}\Psi_e(u,\varphi) &= \left[{}^{t}K_{eu}(u)\right]{}^{t}u + \left[{}^{t}K_{ee}\right]{}^{t}\varphi^{f} - {}^{t}\boldsymbol{Q} = 0
\end{aligned}
\tag{5}
$$

where, $u = \{u, v, w, \beta_x, \beta_y\}^T$ is the nodal displacement vector, φ^f is the free nodal electric potential at the piezoelectric elements. K_{uu} is the effective stiffness matrix including linear and nonlinear (first order and second order nonlinear dependence on u) terms, K_{ue}, K_{eu} are the inverse and direct piezoelectric matrices including linear and nonlinear (first order dependence on u) terms, K_{ee} is the effective electric permittivity matrix which includes only linear terms. ${}^{t}R_b$ and ${}^{t}R$ are the body end external force vectors, respectively. The above-described matrices are exhibited below along with their linear and nonlinear components.

$$
\begin{aligned}
&\left[K_{uu}(u)\right] = \left[K_{uu}^{o}\right] + \left[K_{uu}^{L}\right] = \left[K_{uu}^{o}\right] + \left[P_1(u)\right]/2 + \left[P_2\left(u^2\right)\right]/3 \\
&\left[K_{ue}(u)\right] = \left[K_{ue}^{o}\right] + \left[K_{ue}^{L}\right] = \left[K_{ue}^{o}\right] + \left[P_3(u)\right] \\
&\left[K_{eu}(u)\right] = \left[K_{eu}^{o}\right] + \left[K_{eu}^{L}\right] = \left[K_{eu}^{o}\right] + \left[P_4(u)\right]/2 \\
&\left[K_{ee}\right] = \left[K_{ee}^{o}\right] \\
&\left[C\right] = \alpha\left[M\right] + \beta\left[K_{uu}^{o}\right]
\end{aligned}
\tag{6}
$$

where α, β are the Rayleigh damping coefficients.

The second of Eqs. (5) describes the balance of electric charge in the piezoelectric elements. In particular, the $[K_{eu}]u$ term indicates the electric charge generated at piezoelectric elements, $[K_{ee}]\varphi^f$ denotes the charge stored in their inherent capacitance and ${}^{t}Q$ the electric charge extracted from the piezoelectric element into an external electric circuit.

Based on Eqs. (6), in nonlinear vibrations of prestressed structures, the electromechanical charge conversion in the piezoelectric elements may be improved by the nonlinear piezoelectric coupling matrix $[K_{eu}^{L}]$ which produces electric charge in the piezoelectric layers due to the nonlinear stain S_L. Moreover, the nonlinear stiffness terms $[K_{uu}^{L}]$ may also increase the amount of elastic energy available for conversion in piezoelectric elements during nonlinear vibrations.

More details about the linear and nonlinear components of these matrices have been published in a previous work [30].

Solution Schemes for Discretized Coupled Nonlinear Equations of Motion

In this subsection, the solution schemes adopted for solving the coupled nonlinear equations of motion are briefly described. At first, an axial compressive displacement is applied at one end of the piezoelectric composite beam, while the other end remains fixed. This loading stage could be characterized as pseudo-static, as no dynamic loading is exerted in the structure. The method adopted for solving the nonlinear equations is the Displacement Control method, and assuming also that the solution point cannot be directly achieved, the Newton-Raphson iterative technique is implemented to linearize the coupled nonlinear equations at each iteration.

After the end of prestress, the dynamic loading begins when the piezoelectric composite beam is exerted under a base excitation. For that purpose, the trapezoidal rule of Newmark's time integration method is adopted for solving the discrete coupled nonlinear dynamic system of Eqs. (6) at each time step, along with the Newton-Raphson technique[30].

It is important to note, that in Displacement Control method the total axial compressive displacement is applied incrementally. Each increment is expressed as a discrete point in time domain although there is no physical correlation with time, due to the pseudo-static characteristics of the loading.

Thus, the final linearized system of equations, for both Displacement Control and Newmark's time integration method, is:

$$
\begin{aligned}
\left[{}^{t}\bar{K}_{uu}\left(u^i\right)\right]\Delta u^{i+1} + \left[{}^{t}\bar{K}_{ue}\left(u^i\right)\right]\Delta\varphi^{f^{i+1}} &= -{}^{t}\Psi_u^i\left(u^i, \varphi^i\right) \\
\left[{}^{t}\bar{K}_{eu}\left(u^i\right)\right]\Delta u^{i+1} + \left[{}^{t}\bar{K}_{ee}\right]\Delta\varphi^{f^{i+1}} &= -{}^{t}\Psi_e^i\left(u^i, \varphi^i\right)
\end{aligned}
\tag{7}
$$

where the tangential matrices indicated with the overbar are presented below:

$$\begin{aligned}
&\left[\bar{K}_{uu}(u)\right]=\frac{4}{\Delta t^2}[M]+\frac{2}{\Delta t}[C]+\left[\bar{K}_{uu}^{o}\right]+\left[\bar{K}_{uu}^{\sigma}\right]+\left[\bar{P}_1(u)\right]+\left[\bar{P}_2\left(u^2\right)\right]\\
&\left[\bar{K}_{ue}(u)\right]=\left[\bar{K}_{ue}^{o}\right]+\left[\bar{K}_{ue}^{L}\right]=\left[\bar{K}_{ue}^{o}\right]+\left[\bar{P}_3(u)\right]\\
&\left[\bar{K}_{eu}(u)\right]=\left[\bar{K}_{eu}^{o}\right]+\left[\bar{K}_{eu}^{L}\right]=\left[\bar{K}_{eu}^{o}\right]+\left[\bar{P}_4(u)\right]\\
&\left[\bar{K}_{ee}\right]=\left[\bar{K}_{ee}^{o}\right]
\end{aligned} \tag{8}$$

The stress stiffness matrix K_{uu}^{σ} includes the effect of initial linear mechanical and piezoelectric stresses in the tangential stiffness matrix. In case of Displacement Control, the mass and damping matrices [M], [C] in Eqs. (5)-(8) are not considered, whereas in the Newmark's method these matrices are calculated. Detailed information about the Newmark's method can be found in previous work[30].

3. EXPERIMENTAL APPROACH

3.1 Experimental configuration for nonlinear electromechanical response

A special experimental setup was built to enable dynamic tests on axially loaded composite beams. The experimental setup is illustrated in Figure 1. The setup consists of a horizontal platform made of aluminum, which is capable to oscillate laterally on a pair of horizontal slides. A pair of vertical steel supports are mounted on the base. On the right vertical corner (see Figure 1) there is the mount where the specimen is placed directly. On the other end the vertical steel corner block is mounted on micrometer stage, providing accurate application of horizontal displacement to the specimen. Additionally, the left mount is also equipped with a static canister load cell capable of measuring the axially generated force due to horizontal compression of the specimen from the mechanism. Finally, the left mount of the specimen is directly and rigidly mounted on the load cell. Using the current setup, the specimen is mounted under clamped-clamped boundary conditions. The whole setup is oscillated laterally via an electromechanical shaker mounted on the horizontal platform with simply intervening a dynamic load cell to record the applied force from the shaker on the specimen. Additionally, there is a pair of accelerometers mounted on the horizontal platform and the specimen, respectively. The pair of accelerometers was used in order to extract the net specimen acceleration.

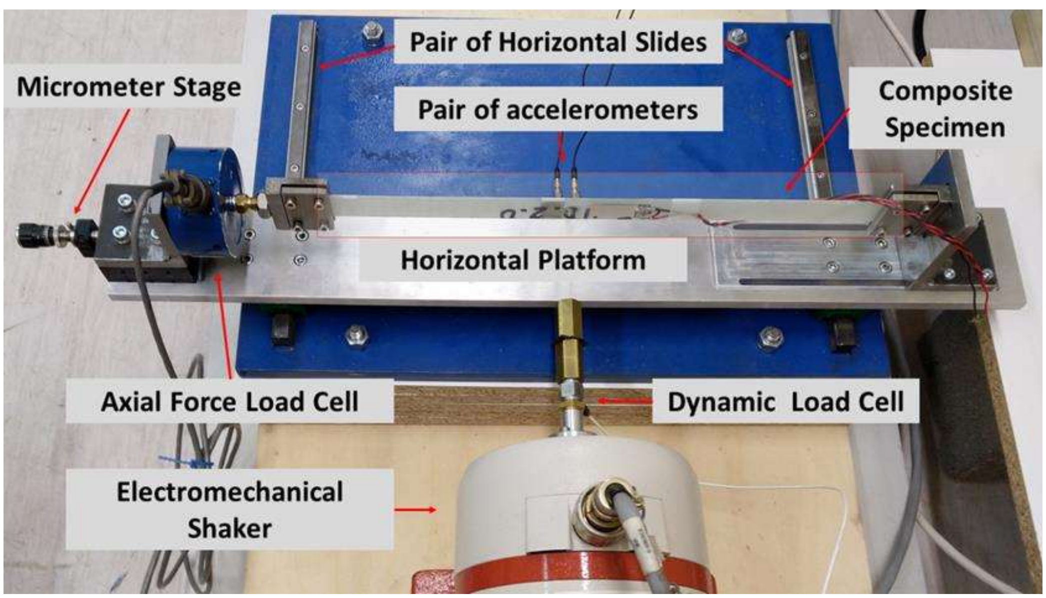

Figure 1. Experimental setup.

3.2 Piezoelectric Energy Harvesting circuits

Three types of PEH circuits have been studied: i) in-house (cc-ih), ii) custom, using off-the-shelf commercial hardware (cc-ch) and iii) commercial, designated as E-821.00 by PI (cc-PI)[26]. In addition, for validation purposes of the numerical methodologies presented in Section 2, measurements have been performed on a resistive circuit (cc-R) and an open-circuit configuration (oc). In the above notation "cc" denotes closed circuit. Each PEH circuit is explicitly described in the following paragraphs.

3.2.1 In-house PEH circuit (cc-ih)

The in-house harvesting circuit, see Figure 2, consists of a diode rectifier due to the alternating input current, a capacitor which charges accumulating electric current and a load with a switch which discharges the capacitor. The coupled electromechanical system serves as a current source via the piezoelectric patch, thus ensuring constant current for charging the capacitor. Consequently, the capacitor may be discharged in a controlled manner to a battery.

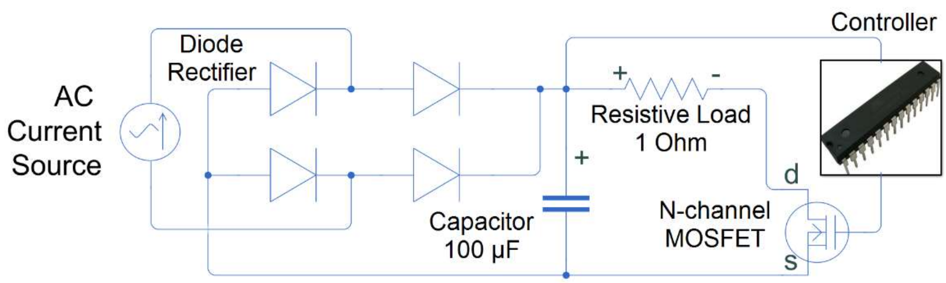

Figure 2. Schematic representation of the cc-ih PEH circuit.

3.2.2 Custom commercial PEH (cc-ch)

The custom commercial PEH circuit includes an SPV1050 energy harvester[27], a STEVAL-ISV020V1 evaluation board and a battery charger. The SPV1050 is an ultralow power, high-efficiency energy harvester and battery charger, which implements the maximum power point tracking function (MPPT) and integrates the switching elements of a buck-boost converter. However, the SPV1050 lacks the rectifying stage needed for piezoelectric sources, as it is intended for PV applications. In order to enable its use for the current application a full-wave rectifier has been designed and implemented, which additionally includes a Zener diode for protection of the integrated circuit against voltage overshooting. The custom commercial circuitry and board are shown in Figure 3.

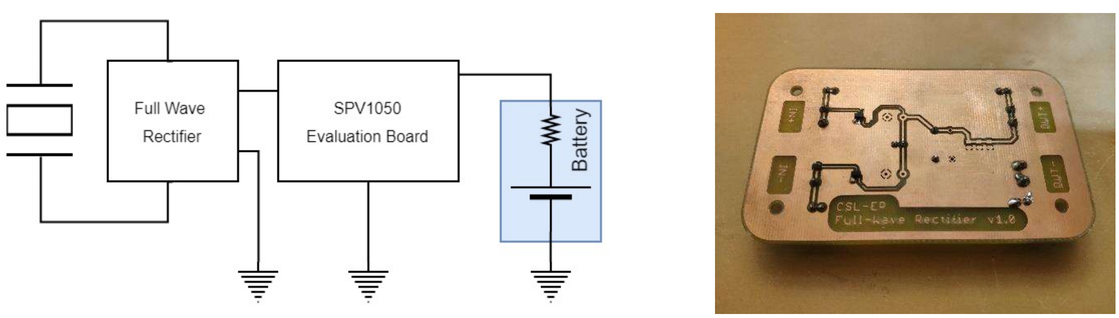

Figure 3. Custom commercial PEH circuitry and board.

3.2.3 Commercial PEH (cc-PI)

The commercial circuit E-821.00 manufactured by PI is an integrated circuit that includes a diode rectifier and a capacitor that charges due to the alternative current produced by the piezoelectric crystal. When the voltage of the capacitor reaches the 12V mark, an automatic switch is activated which allows part of the electrical energy in the capacitor to be released into a secondary sub-circuit. The automatic switch is turned off when the voltage of the capacitor falls at 6V. The switch is implemented by a MOSFET controlled by an operational amplifier which compares the voltage of the capacitor to a reference voltage. The secondary circuit consists of a buck converter and voltage clipper that assures that the output of E-821.00 is a pulse of constant voltage. The commercial PEH circuit is shown in Figure 4.

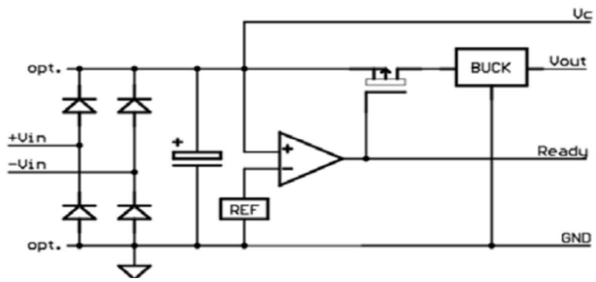

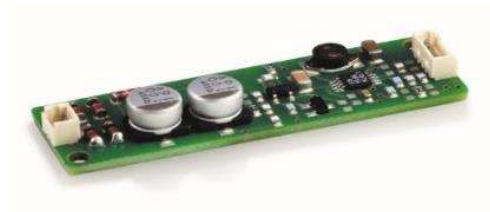

Figure 4. Commercial PEH circuit and board.

4. RESULTS AND DISCUSSION

4.1 Open-circuit (OC) response

Performance of the numerical tool

The 1st part of the experimental study focuses on the investigation of the performance of the developed numerical tool correlated with the described experimental facility. Simulations and measurements were performed on a composite beam equipped with a pair of piezopolymer sensors. The specimen was simulated under clamped-clamped boundary conditions (Figure 1) having 366 mm free length, 20 mm width and 2.4mm thickness, while it was made of Gl/Epoxy with $[0]_3$ laminate configuration (material properties are shown in Table 1). Additionally, there was a concentrated 5g mass. The FE mesh density was 20x1 elements for all numerical cases.

Table 1. Mechanical properties of Gl/Epoxy composite beam.

Property	Composite Material
Density (kg/m^3)	1951.5
E_{11} (GPa)	41.45
E_{22} (GPa)	12.5
E_{33} (GPa)	12.5
G_{12} (GPa)	4.55
G_{13} (GPa)	4.55
G_{23} (GPa)	4.46
ν_{12}	0.348
ν_{13}	0.348
ν_{23}	0.4

During the experimental procedure the specimen was axially loaded by applying displacement via the left mounted micrometer stage (Figure 1). The loading was interrupted in steps of axially generated force on the static load cell and a modal testing was performed on the specimen with lateral mechanism excitation via the electromechanical shaker. The actuation signal was a swept sine in the range 0 to 100 Hz with 13.2 s duration and during the actuation the acceleration was acquired by the pair of accelerometers to provide the net specimen acceleration. FRFs were extracted using the net specimen acceleration and the measured force through the dynamic load cell. Fitting the FRFs with a numerical tool based on complex and exponential terms the modal frequency of the specimen's 1st bending mode was extracted. Similar simulations were performed using the numerical tool. The correlations between the numerical simulation and the experimental measurements were performed for the static stable buckling path and the corresponding variation of the small-amplitude fundamental modal frequency of the beam and are shown in Figure 5 (a) and (b) respectively.

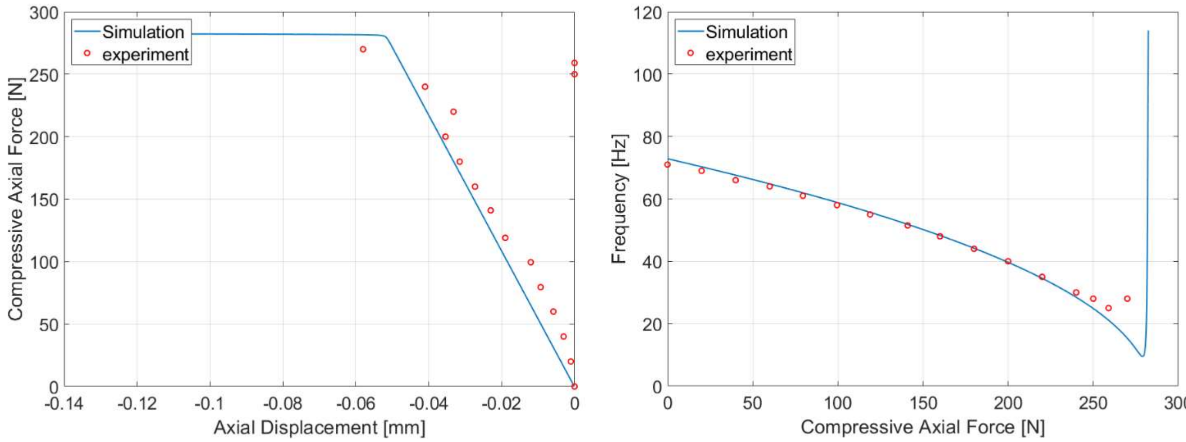

Figure 5 (a) Static response of the piezoelectric composite beam under axial compressive displacement and (b) Small amplitude vibration response of the piezoelectric composite beam under axial compressive displacement.

According to the previous Figures, an excellent correlation is presented between experimental measurements and simulations, especially in Figure 5 (b). The only noticeable difference among the results take place near the critical buckling load value, which was calculated at 279 N (where the fundamental frequency of the beam reaches the minimum point), while experimentally was about 260 N. This difference was deemed to be the outcome of an initial imperfection in the physical beam which may not be easily quantified, yet it plays a significant role in a region close to buckling.

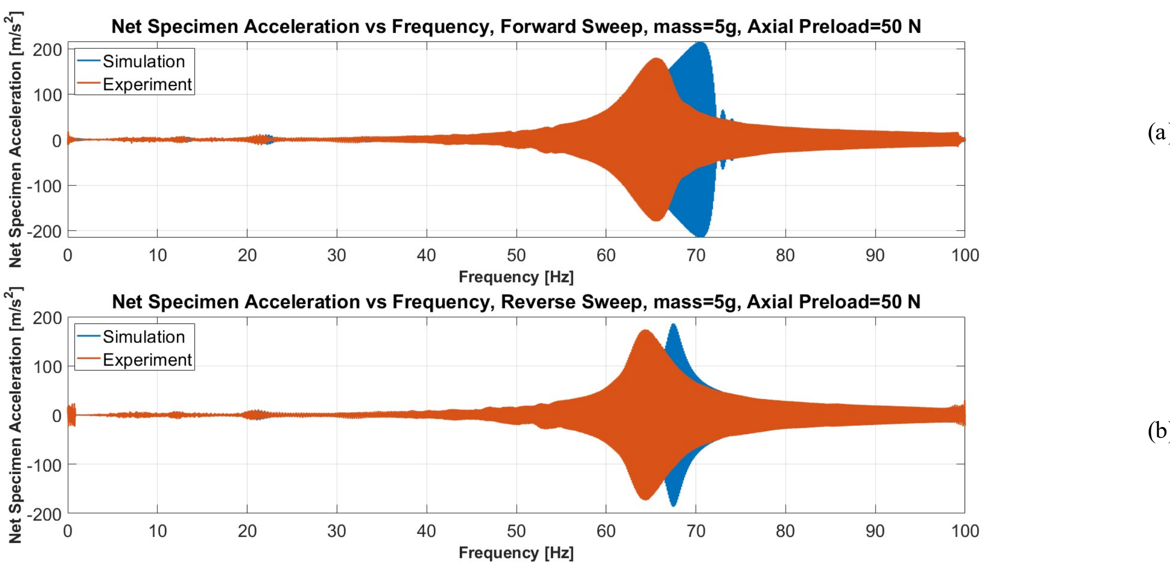

Figure 6. (a) Predicted and measured net acceleration of the transversely vibrated piezoelectric beam in prebuckling regime subjected to 50 N axial preload, under forward 0→100Hz sweeping base acceleration (b) Predicted and measured net acceleration of the transversely vibrated piezoelectric beam in prebuckling regime subjected to 50 N axial preload, under reverse 100→0Hz sweeping base acceleration

The next step following the agreement between the numerical and experimental results at pseudo-static loading and small amplitude vibration response was the validation of the specimen dynamic response under base excitation. As described in the previous case loading was interrupted in steps of 50N and for every step a swept sine base excitation was applied with shaker amplitude selected in the manner that generates 1g magnitude of the base acceleration. Two different swept sine signals were applied the forward with increasing frequency (0→100Hz) and reverse sweep decreasing frequency (100→0Hz). To perform representative simulations the measured base acceleration was applied as input to the computational tool performing the actuation signal and simulating the composite beam transient response. Correlations are presented in Figure 6 and Figure 7, for 50N and 200N axial load to the specimen respectively.

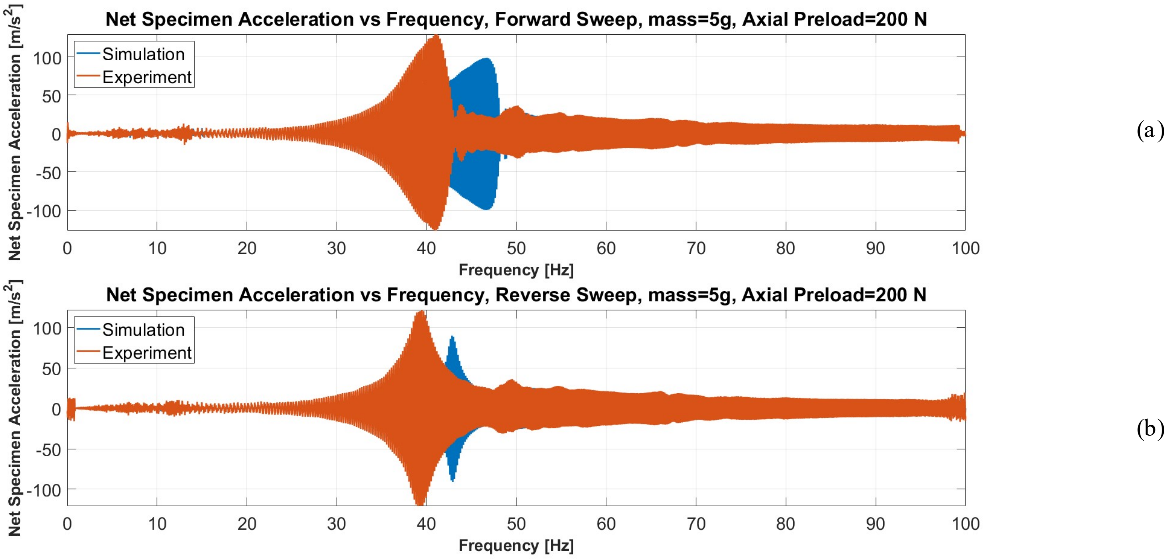

Figure 7. (a) Predicted and measured net acceleration of the transversely vibrated piezoelectric beam in prebuckling regime subjected to 200 N axial preload, under forward 0→100Hz sweeping base acceleration (b) Predicted and measured net acceleration of the transversely vibrated piezoelectric beam in prebuckling regime subjected to 200 N axial preload, under reverse 100→0Hz sweeping base acceleration

These figures present the variation of the specimen net acceleration within the range of sweep actuation, capturing the increase to the specimen acceleration during the excitation of the 1st bending modal frequency. Each Figure contains a pair of graphs, the 1st presenting the increasing sweeping actuation and the 2nd the backwards actuation. Generally, very good agreement is presented between numerical and the experimental results. Noticeable differences are related to the ability of the model to simulate accurately the maximum amplitude and the exact frequency of the specimen oscillation at the zone of modal frequency. As presented in Figures 7 and 8, a very good agreement was captured between simulation and experiment away from the range of the modal frequency. Near the modal frequency there is some shifting between experimental and numerical results which is attributed to two effects not sufficiently captured by the present model: (1) differences between the actual and modelled initial imperfections of the strip which seem to affect the onset of nonlinearities in the vibration due to large rotations. (2) limitation of the Rayleigh Damping scheme to model the real physical damping of the composite strip, which previous studies have shown to be highly sensitive to the pre-stress load and buckling state[31]. However, it is worth mentioning that the oscillation amplitude decreases suddenly after the sweep excitation crosses the zone of the 1st bending mode. This behaviour becomes more severe as the compressive load increases, is duplicated from both measurements and simulations, and appears only in forward sweeping actuation.

The next case study focuses to the correlation of the net specimen acceleration between the experimental and numerical results in the case of constant excitation frequency. Similar to the previous case, the specimen axial loading was interrupted in steps of 50N axial force and a constant sinusoidal actuation signal was applied from the shaker at 50Hz resulting to 1g sinusoidal base acceleration amplitude. Also, the measured base acceleration provided the transient response simulation actuation signal in the same manner described in the previous case. Figure 8 (a) and (b) present the correlation between measurement and simulation of the net acceleration of the specimen. The dynamic response from both simulations and experiment are presented after a short period in the manner that the transient phenomena are eliminated. Correlations present an excellent agreement between model and experiment. Especially correlations of Figure 8 (b), presenting the oscillatory specimen behaviour almost 50N before the critical buckling load indicate the model efficiency to describe the nonlinear structural response. These results indicate the model efficiency to accurately simulate the static and dynamic response of a composite beam under various actuation signals and during the axial loading.

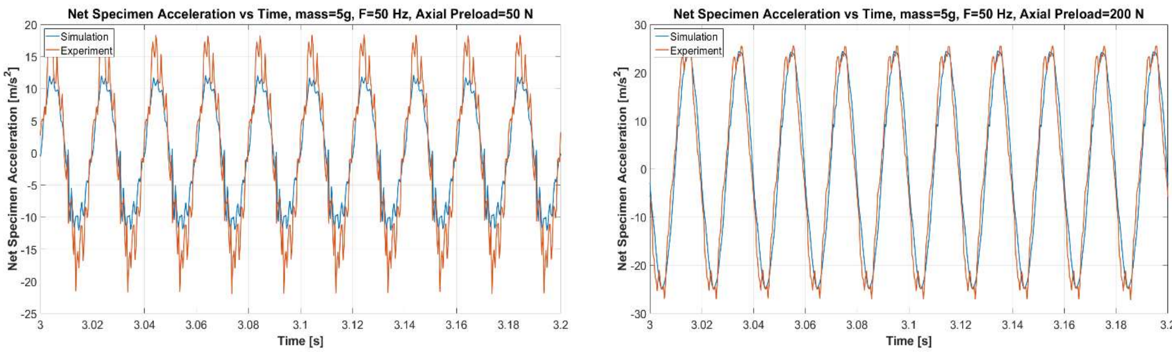

(a) (b)

Figure 8. Predicted and measured net acceleration of the transversely vibrating piezoelectric beam under 50 Hz sinusoidal base oscillation in the prebuckling regime and subjected to (a) 50 N and (b) 200N axial preload.

Simulations of the sensory voltage

This case study presents solely simulations of the generated sensory voltage. The composite beam, identical to the one used during the previous cases was simulated with a special, compliant DuraAct, piezoelectric device (P-876.A12 of PI). Considering the increased stiffness of the beam due to the piezoceramic presence, the variation of the small-amplitude fundamental modal frequency as a function of the applied axial load is presented in Figure 9 capturing a small increase in the critical buckling load and modal frequencies.

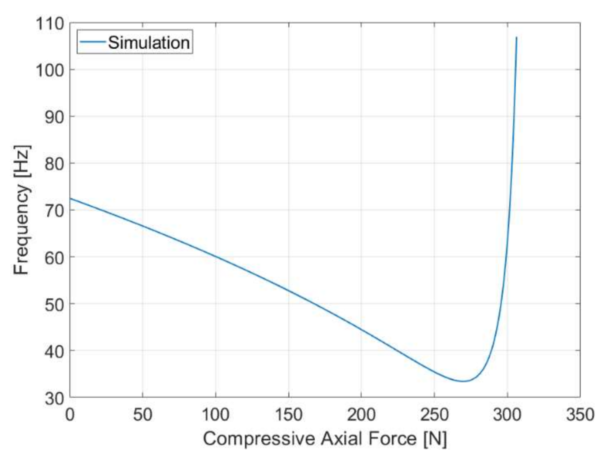

Figure 9. Small amplitude vibration response of the piezoelectric composite beam under axial compressive displacement.

In Figure 10, both the generated electrical voltage (a) at the terminals of the special compliant piezoceramic sensor as well as the net specimen acceleration (b) are presented as a function of the duration of the swept sine excitation. Similar to the previous cases the piezoelectric composite beam response was simulated for base forward swept sine excitation frequency (0→100Hz) and the simulations presented in the aforementioned figure are for 250 N axial compressive load. Both curves exhibit the same period of time where their amplitudes appear to increase, with the maximum value occurring at the same time. Thus, it is deduced that the generated voltage across the piezoelectric material terminals follows the net acceleration amplitude trend.

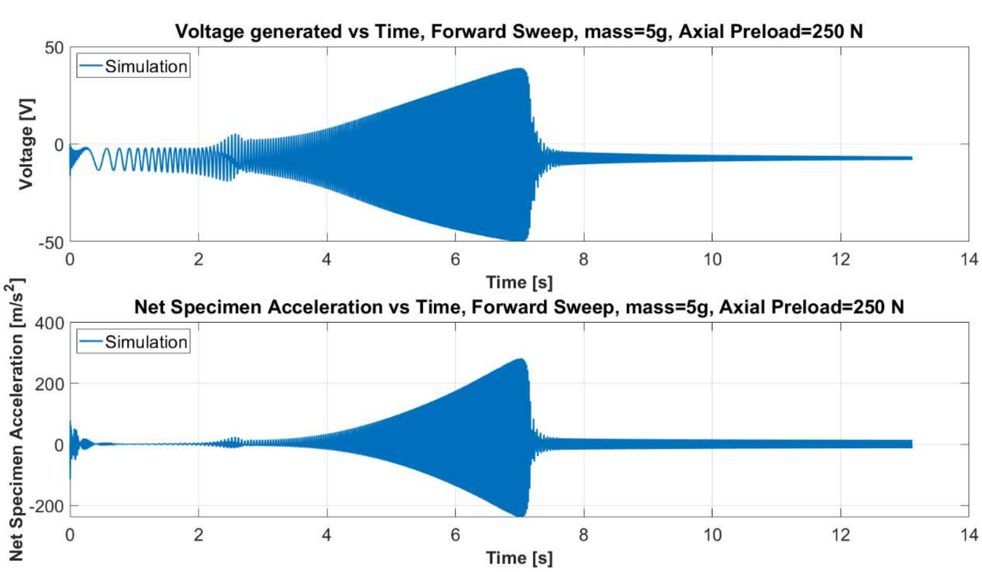

(a)

(b)

Figure 10. Time response of (a) the generated voltage and (b) the acceleration of the transversely oscillated piezoelectric beam due to the base acceleration for 250 N axial preload and a forward swept excitation frequency (0→100Hz).

The last study of the open circuit response investigates the effect of the prestress level on the voltage generated at the terminals of the piezoceramic sensor. Each of the three plots of Figure 11 present the predicted sensory voltage for 0, 150 and 250N axial compressive force respectively. All three plots were generated for the same base excitation signal. The first obvious conclusion is the predicted increase in the range and the lower frequency range of the sensory voltage oscillation, as the prestress increases. This suggests improved electromechanical conversion due to the increase of the nonlinearity in the oscillated structure. Additionally, the increase appears to be nonlinear as the load approaches the critical buckling load. Finally, it is worth mentioning the fact that the numerical model is capable to capture the specimen imperfection due to loss of symmetry through-the-thickness and induced bending-extension coupling in the specimen, as the piezoelectric is bonded only from the one side of the specimen. This is illustrated at the figures by the asymmetric oscillation of the voltage and its offset from the 0 Volts.

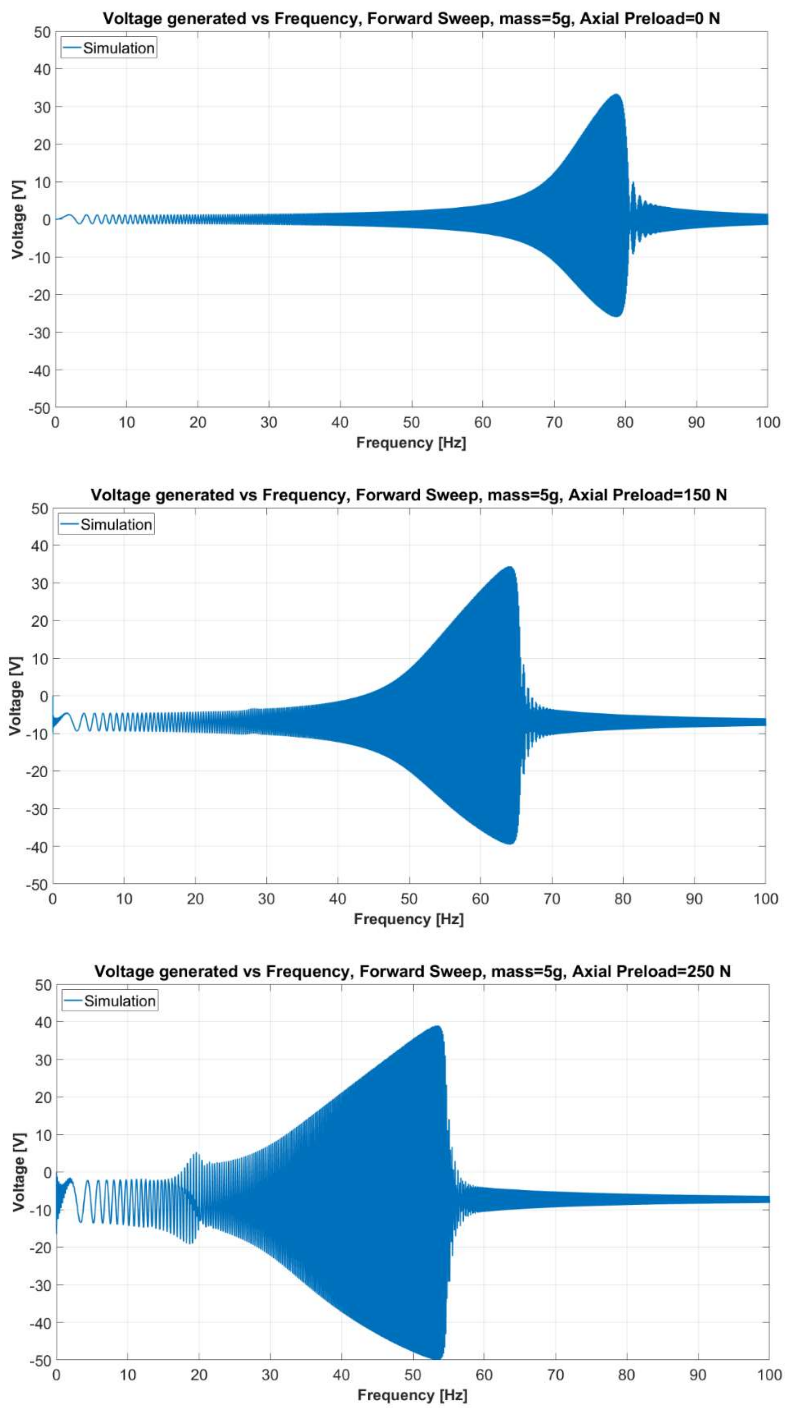

(a)

(b)

(c)

Figure 11. The generated voltage at the terminals of the DuraAct piezoelectric sensor under forward swept base excitation frequency (0→100Hz) and (a) 0 N (b) 150N and (c) 250N axial preload in prebuckling regime.

4.2 Closed Circuit (CC) response

Current section presents the investigation of the closed circuitry performance of the electromechanical prototype described in the previous section. The composite beam used for this study has identical properties, is equipped with the same Dura Act sensor and the only difference was the composite beam width, which was 30mm. Four different circuits were connected at the terminals of the piezoceramic. The 1st consisted of a resistive load, while the other 3 were harvesting circuits; (a) an in-house, (b) a modified commercial and (c) an off-the-shelf solution.

Closed-circuit response with electric resistance (CC-R)

In Figure 12a and b the effect of excitation frequency on voltage and current measured at a resistive load of 11.9 kΩ connected to the piezoelectric patch is shown. The beam is subjected to 100 N axial load and vibrates under a base excitation of 1g. The eigenfrequency of the beam under the current loading conditions is at 84 Hz. Thus, excitation at 80 Hz leads to higher voltage, as expected. The relatively high power produced near resonance (in the order of tens of mW) should be also noted in this case.

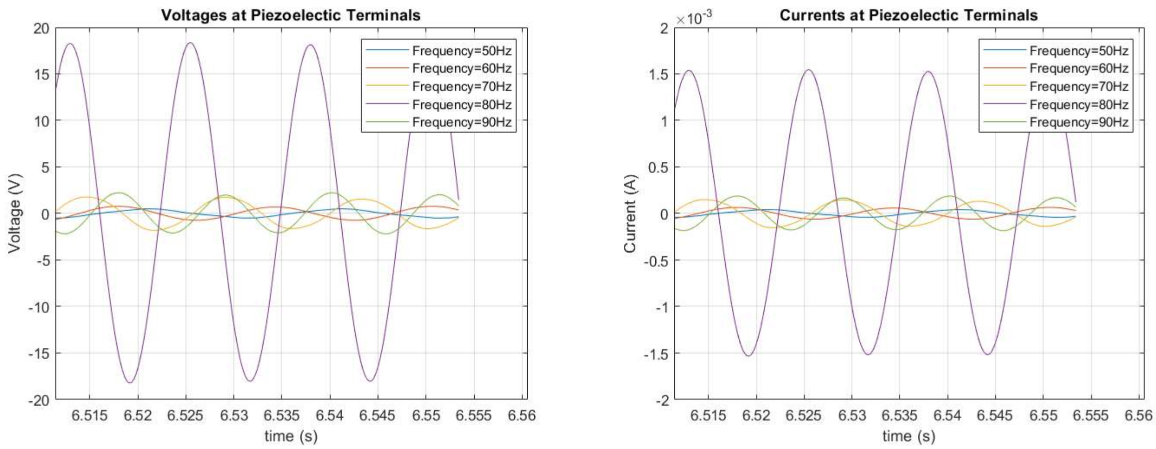

(a) (b)

Figure 12. Effect of excitation frequency on resistive voltage and current derived in a closed-circuit configurated vibrating beam subjected to an axial load of 100 N.

Closed-circuit response with harvesting circuits

As observed in the previous experimental sections, the most efficient excitation frequency is near the eigenfrequency of the beam, around 80 Hz. Thus, all harvesting circuits have been tested under sinusoidal excitation at this frequency. The axial compressive load remains 100 N and the applied load results to magnitude 1g base acceleration.

In Figure 13 output voltage and current at the in-house harvesting circuit (cc-ih) connected to the patch are presented. Concerning voltage, the charging circuit switch on/off thresholds can be extracted from Figure 13a.

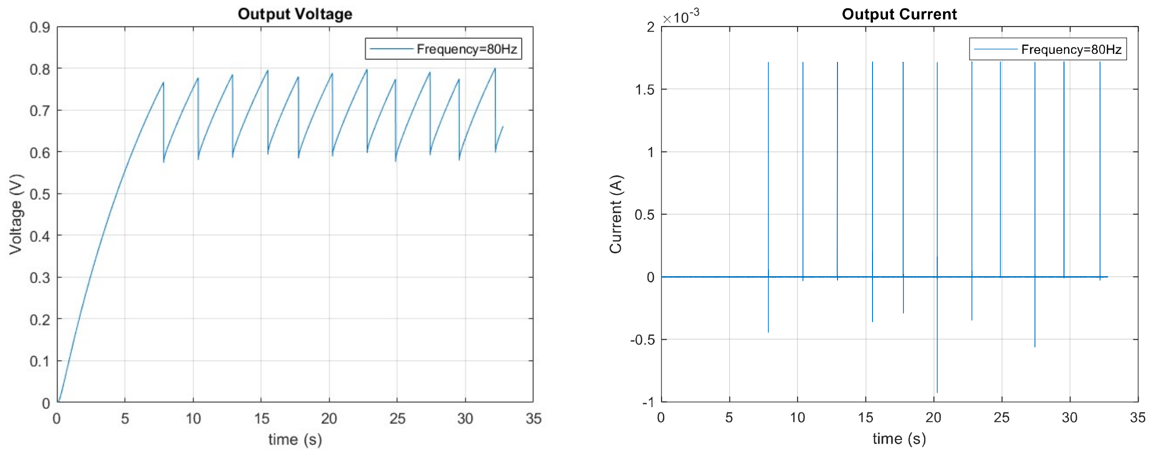

(a) (b)

Figure 13. Response of in-house harvesting circuit (cc-ih).

The response of the modified commercial harvesting circuit (cc-ch) is shown in Figure 14a-b. Compared to the in-house circuit the higher frequency of power extraction should be noted, as indicated by the timescale of the current time signal. This circuit proved to be most prominent in terms of harvested power.

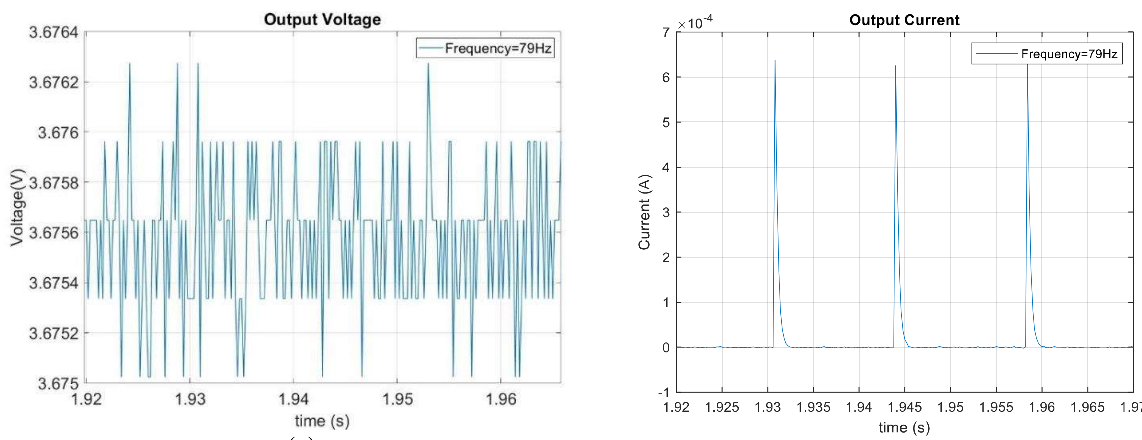

(a) (b)

Figure 14. Response of modified commercial harvesting circuit (cc-ch).

The response of the commercial harvesting circuit (cc-PI) is shown in Figure 15a-b. Figure 15a presents the voltage response at the capacitor of the charging circuit and reveals that the threshold for discharging into the battery never got reached.

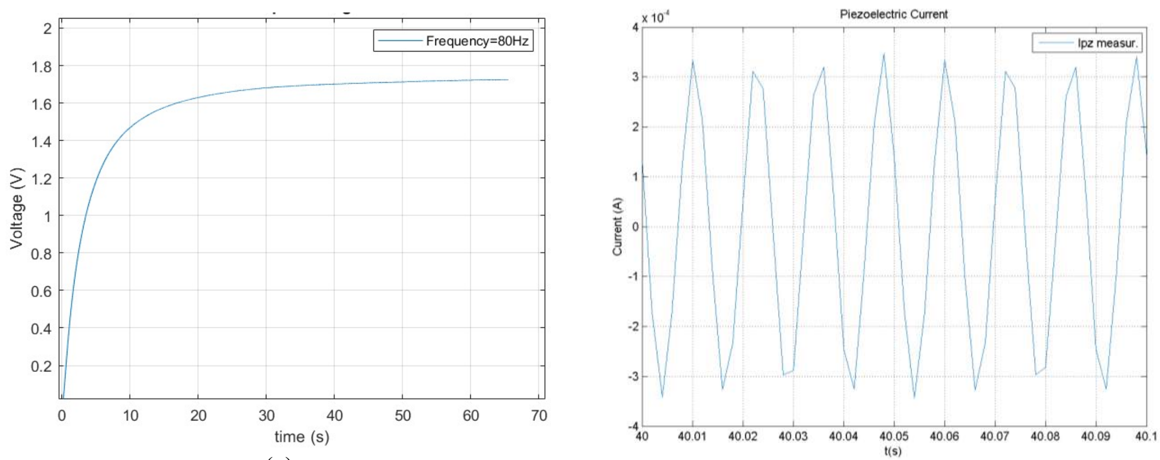

(a) (b)

Figure 15. Response of commercial harvesting circuit (cc-PI): a) voltage at capacitor, b) current snapshot through charging circuit.

At a first comparison approach of the three harvesting circuits on the basis of these preliminary measurements some general observations may be summarized as follows: i) the modified commercial circuit appears to harvest most power, ii) a major advantage of the in-house harvesting circuit is its capability to harvest energy in a much wider range of external load and excitation frequency compared to the other two, iii) the maximum harvested power appears to be in the range of tens of mW, which is a considerable amount for IoT applications.

5. CONCLUDING REMARKS

A computational nonlinear structural dynamics framework, including stress stiffening and large rotations effects, was expanded to predict the nonlinear coupled dynamic electromechanical response. The dynamic response was demonstrated in terms of acceleration and electric voltage, of prestressed vibrating beams with attached piezoelectric sensors. This model provides the basis for designing and tailoring the parameters of an electromechanical setup ideal for energy production from oscillated beams. Additionally, a prototype experimental setup was built based on the idea of electrical energy production from a transversely oscillated beam subjected to axial load till the critical buckling state. The experimental apparatus initially provided the required computational tool validations, first in the range of linearized small amplitude vibrations and subsequently under highly nonlinear dynamic oscillations in the prebuckling regime. Furthermore, its performance was studied under open and closed-circuit conditions. The OC simulations presented a nonlinearly increased electrical voltage generation at the terminals of the piezoceramic sensor. This observation agreed with the prototype design assumption based on the energy production due to geometrical nonlinearity. On behalf of the CC response performance, three different circuits were studied experimentally, and presented potential to generate some power from the oscillated structure, but the obtained results are considered to be still preliminary and require further investigation. In any case the harvested power range has been quantified and the capabilities/shortcomings of each circuit have been recognized in order to proceed to the development of a successful prototype.

ACKNOWLEDGEMENT

This research has been co-financed by the European Regional Development Fund of the European Union and Greek national funds through the Operational Program Competitiveness, Entrepreneurship and Innovation, under the call RESEARCH – CREATE – INNOVATE (project code: T1EDK-01533).

REFERENCES

[1] Harne, R. L. and Wang, K. W., "A review of the recent research on vibration energy harvesting via bistable systems," Smart Materials and Structures 22(2), 1-12 (2013).

[2] Jia, Y., "Review of nonlinear vibration energy harvesting: Duffing, bistability, parametric, stochastic and others," Journal of Intelligent Material Systems and Structures 31(27), 921-944 (2020).

[3] Mann, B. P. and Sims, N. D., "Energy harvesting from the nonlinear oscillations of magnetic levitation," Journal of Sound and Vibration 319(1-2), 515-530 (2009).

[4] Wickenheiser, A. M. and Garcia, E., "Broadband vibration-based energy harvesting improvement through frequency up-conversion by magnetic excitation," Smart Materials and Structures 19(6), 1-11 (2010).

[5] Erturk, A. and Inman, D. J., "Broadband piezoelectric power generation on high-energy orbits of the bistable Duffing oscillator with electromechanical coupling," Journal of Sound and Vibration 330(10), 2339-2353 (2011).

[6] Karami, M. A. and Inman, D. J., "Analytical modeling and experimental verification of the vibrations of the zig zag microstructure for energy harvesting," Journal of Vibration and Acoustics 133(1), 1-10 (2011).

[7] Ansari, M. H. and Karami, M. A., "Experimental investigation of fan-folded piezoelectric energy harvesting for powering pacemakers," Smart Materials and Structures 26(6), 1-9 (2017).

[8] Masana, R. and Daqaq, M. F., "Energy harvesting in the super-harmonic frequency region of a twin-well oscillator," Journal of Applied Physics 111(4), 1-11 (2012).

[9] Autonomous data acquisition and wireless transmission system based on piezoelectric energy harvesting. Research-Create-Innovate project T1EDK-01533, https://www.enausi-project.gr/en.

[10] Leland, E. S. and Wright, P. K., "Resonance tuning of piezoelectric vibration energy scavenging generators using compressive axial preload," Smart Materials and Structures 15(5), 1413-1420 (2006).

[11] Sneller, A. J., Cette, P. and Mann, B. P., "Experimental investigation of a post-buckled piezoelectric beam with an attached central mass used to harvest energy," Proceedings of the Institution of Mechanical Engineers, Part I: Journal of Systems and Control Engineering 225(4), 497-509 (2011).

[12] Masana, R. and Daqaq, M. F., "Electromechanical modeling and nonlinear analysis of axially loaded energy harvesters," Journal of Vibration and Acoustics 133(1), 1-10 (2011).

[13] Cottone, F., Gammaitoni, L., Vocca, H., Ferrari, H. and Ferrari, V., "Piezoelectric buckled beams for random vibration energy harvesting," Smart Materials and Structures 21(3), 1-11 (2012).

[14] Ramlan, R., Brennan, M. J., Mace, B. R. and Kovacic, I., "Potential benefits of a non-linear stiffness in an energy harvesting device," Nonlinear Dynamics 59(4), 545-558 (2010).

[15] Liu, W. Q., Badel, A., Formosa, F., Wu, Y. P. and Agbossou, A., "Novel piezoelectric bistable oscillator architecture for wideband vibration energy harvesting," Smart Materials and Structures 22(3), 1-11 (2013).

[16] Liu, W., Formosa, F., Badel, A. and Hu, G., "A simplified lumped model for the optimization of post-buckled beam architecture wideband generator," Journal of Sound and Vibration 409, 165-179 (2017).

[17] Wu, L., Do, X. D., Lee, S. G. and Ha, D. S., "A self-powered and optimal SSHI circuit integrated with with an active rectifier for piezoelectric energy harvesting," IEEE Transactions on Circuits and Systems I: Regular Papers 64(3), 537-549 (2016).

[18] Ottman, G. K., Hoffmann, H. F., Bhatt, A. C. and Lesieutre, G. A., "Adaptive piezoelectric energy harvesting circuit for wireless remote power supply," IEEE Transactions on Power Electronics, 17(5), 669-676 (2002).

[19] Lefeuvre, E., Audigier, D., Richard, C. and Guyomar, D., "Buck-boost converter for sensorless power optimization of piezoelectric energy harvester," IEEE Transactions on Power Electronics, 22(5), 2018-2025 (2007).

[20] Lallart, M., Garbuio, L., Petit, L., Richard, C. and Guyomar, D., "Double synchronized switch harvesting (DSSH): a new harvesting scheme for efficient energy extraction," IEEE Transactions on Ultrasonics, Ferroelectrics, and Frequency Control, 55(10), 2119-2130 (2008).

[21] Shen, H., Qiu, J., Ji, H., Zhu, K. and Balsi, M., "Enhanced synchronized switch harvesting: a new energy harvesting scheme for efficient energy extraction," Smart Materials and Structures, 19(11), 1-14 (2010).

[22] Ramadass, Y. K. and Chandrakasan, A. P., "An efficient piezoelectric energy harvesting interface circuit using a bias-flip rectifier and shared inductor," IEEE Journal of Solid-State Circuits, 45(1), 189-204 (2010).

[23] Tabesh, A. and Frechette, L. G., "A low-power stand-alone adaptive circuit for harvesting energy from a piezoelectric micropower generator," IEEE Transactions on Industrial Electronics 57(3), 840-849 (2010).

[24] Liang, J. and Liao, W. H., "Impedance modeling and analysis for piezoelectric energy harvesting systems," IEEE/ASME Transactions on Mechatronics, 17(6), 1145-1157 (2012).

[25] Huguet, T., Lallart, M. and Badel, A., "Bistable vibration energy harvester and SECE circuit exploring their mutual influence," Nonlinear Dynamics 97(5), 485-501 (2019).
[26] E-821 Electronic module for energy harvesting using piezo actuators for energy generation. PI Motion/Positioning, 2014.
[27] Datasheet SPV1050 Ultralow power energy harvester and battery charger. STMicroelectronics, 2018.
[28] Varelis, D. and Saravanos, D. A., "Mechanics and finite element for nonlinear response of active laminated piezoelectric plates," AIAA Journal 42(6), 1227-1235 (2004).
[29] Varelis, D. and Saravanos, D. A., "Coupled finite element for the nonlinear dynamic response of active piezoelectric plates under thermoelectromechanical loads," J. Mech. Mater. Struct. 4(7), 1489-1503 (2009).
[30] Varelis, D., Kardarakos, G.-C., Chrysochoidis, N. and Saravanos, D. A., "Towards a nonlinear buckled piezoelectric beam system for enhanced electromechanical energy conversion," Proc. SPIE 11376, 1-17 (2020).
[31] Chortis, D. I., Varelis, D. S. and Saravanos, D. A., "Linearized frequencies and damping in composite laminated beams subject to buckling," Journal of Vibration and Acoustics 135(2), 1-10 (2013).